This is a preprint of the following article, which is available from http://mdolab.engin.umich.edu
Gustavo L. O. Halila, Anil Yildirim, Charles A. Mader, Krzysztof J. Fidkowski, Joaquim R. R. A. Martins, Linear Stability-Based Smooth RANS Transition Model for Aerodynamic Flows. *AIAA Journal*, 2021.
The published article may differ from this preprint, and is available by following the DOI: https://doi.org/10.2514/1.J060481.

Linear Stability-Based Smooth RANS Transition Model for Aerodynamic Flows

Gustavo L. O. Halila, Anil Yildirim, Charles A. Mader, Krzysztof J. Fidkowski, Joaquim R. R. A. Martins
Department of Aerospace Engineering, University of Michigan, Ann Arbor, MI, 48109

Abstract

The inclusion of transition to turbulence effects in computational fluid dynamics (CFD) simulations makes it possible to design laminar flow airframes. It also increases the level of physical representations for simulations of standard airframes because laminar flow regions may be present in parts of the aircraft in multiple flight conditions. Modified Reynolds-averaged Navier–Stokes (RANS) models that consider transition effects became popular in the last decade and indicated favorable agreement with experimental data. However, these models present more difficult convergence behavior when compared to fully turbulent RANS approaches. To address this issue, we leverage an approximate Newton–Krylov solver to solve the transitional flow over aeronautical configurations using a flow stability-based, smooth RANS transition model. The amplification factor transport (AFT) model is modified to create a smooth variant, referred to as AFT-S. We developed strategies to obtain representative physical solutions that exhibit good agreement with experimental data. We also address the convergence behavior for the transition RANS model and assess its impact on the numerical results. These results constitute the first in-depth investigation on the numerical behavior of an AFT-type transition model.

Nomenclature

c_f	=	Skin friction coefficient
d	=	Distance from the wall
δ_1	=	Boundary layer displacement thickness
γ	=	Intermittency
$\tilde{\gamma}$	=	$\ln(\gamma)$, modified intermittency

H_{12} = Boundary layer shape factor
H_L = Local shape factor
$\mathcal{I}$ = Identity matrix
$\mathcal{M}$ = Preconditioner matrix
N = $\ln(A/A_0)$, amplification factor
N_{crit} = Critical N-factor
$\tilde{n}$ = Approximate N-factor
$\mathcal{Q}$ = State vector
$\mathcal{R}$ = Residual equations
Re_θ = Momentum thickness Reynolds number
R_T = μ_t/μ, turbulent Reynolds number
S = Strain rate magnitude
Tu = Freestream turbulence intensity
x_j = Spatial coordinates
μ = Molecular dynamic viscosity
μ_t = Eddy viscosity
$\tilde{\nu}$ = Spalart–Allmaras turbulence model working variable
Ω = Vorticity magnitude
θ = Boundary layer momentum thickness
ρ = Density

Subscripts

∞ = Freestream

1 Introduction

In computational fluid dynamics (CFD), cost-effective transitional flow simulations can be achieved using flow stability analysis or modified Reynolds-averaged Navier–Stokes (RANS) turbulence models. In flow stability analysis, the stability wave modes superimposed to a laminar baseflow are tracked in space or time. In previous work, we proposed a robust flow stability framework for aeronautical applications [1]. This framework was coupled to a high-order CFD solver equipped with goal-oriented mesh adaptation [2]. Although flow stability analysis enables a physical interpretation of the flow modes that trigger transition, its combination with CFD solvers results in complex computational frameworks, which may render its application in industrial environments unlikely. RANS turbulence models, commonly used in engineering applications, result from a Favre time-averaging of the original Navier–Stokes equations. As a result, crucial spectral information is missing [3], and no knowledge of the transition to turbulence process is retained. The natural approach to address this shortcoming is to develop an additional model for the transitional region and integrate it into the original turbulence closure. Modeling of transition to turbulence is performed by including additional transport equations, generally supported by empirical correlations. The use of these correlations was first proposed by Abu–Ghannam and Shaw [4], Mayle [5],

and Suzen et al. [6]. These correlations compare the computed momentum thickness Reynolds number, Re_θ, to a threshold value to specify the transition onset. Because the calculation of Re_θ demands non-local operations, such as the integration of the velocity and density profiles along the wall-normal direction inside the boundary layer, it is challenging to implement in parallel CFD codes.

Langtry and Menter [7–10] proposed a transition model where two additional transport equations are used to estimate transition onset and region extent. Transition onset is triggered by the momentum thickness Reynolds number (Re_θ) transport equation, and the intermittency (γ) transport equation is used to estimate the extent of the transition region. The γ-Re_θ model uses empirical correlations to compute the momentum thickness Reynolds number through local variables, making the model practical for parallel CFD codes. The shear stress transport (SST) turbulence model [11] is modified such that the source terms in the turbulent kinetic energy equation are affected by the intermittency field.

A RANS transition model based on linear stability theory was first proposed by Coder and Maughmer [12]. They proposed a transport equation for the approximate N-factor envelope, $\tilde{n}$, based on the work of Drela and Giles [13], with the Spalart–Allmaras (SA) turbulence model [14] as the base for the new two-equation transition model, named amplification factor transport (AFT). The AFT model was then augmented with an additional transport equation for the modified intermittency, $\tilde{\gamma}$, to improve its robustness when complex flows are considered [15].

The correlations for the approximate N-factor originally proposed by Drela and Giles depend on integral boundary layer quantities, such as the shape factor, H_{12}, which is defined as

$$H_{12} = \frac{\delta_1}{\theta}, \tag{1}$$

where δ_1 and θ are, the boundary layer displacement and momentum thicknesses, respectively. The AFT model circumvents this issue by adopting a surrogate, local shape factor, H_L. We highlight that, in the context of RANS transition models, the term non-local refers to the presence of integral boundary layer quantities in the formulation. In contrast, in flow stability analysis, the same term relates to boundary layer history effects in the governing equations. In this paper, the term local indicates that physical quantities represented by integral forms are replaced by surrogates that reproduce the original quantity without performing wall-normal integrations.

Compared with the original Langtry–Menter transition model, the AFT model has three transport equations against four transport equations for the former. This model was proposed as a tool to study external aerodynamic flows, as opposed to the Langtry–Menter model that was originally developed to investigate transitional flows in turbomachinery, where the turbulence levels are higher than those typically found in wind tunnels or free flight.

When transition RANS models are used, it is vital to consider the effect of freestream turbulence variables on the predicted results. In the Langtry–Menter model, additional measures must be taken to avoid the effects of the inflow turbulence variables decay inherent to the SST turbulence model. Spalart and Rumsey [16] proposed model corrections and best practices to address this issue. Halila et al. used turbulence con-

servations boxes, regions of the numerical domain where the turbulence source terms are turned off, to avoid the freestream turbulence properties decay [3, 17]. The critical N-factor is directly correlated to the freestream turbulence intensity in the AFT transition model. Therefore, no additional corrections are needed to correctly correlate wind tunnel or flight turbulence intensities with the transition front location.

While more research groups implement and test the AFT model, some available investigations indicate that it deserves attention as a transition prediction tool. Apart from the results from Coder and Maughmer, Denison and Pulliam [18] showed that transitional flow results obtained by the AFT model are in good agreement with experimental data. Details on the AFT model formulation are provided in Section 2.

The numerical behavior and convergence characteristics are crucial aspects when using modified RANS models that can capture transition to turbulence effects. The correlations that feed source terms in these models are highly nonlinear, introducing obstacles in achieving engineering or machine-zero convergence levels. Piotrowski and Zingg [19] propose a coupled solution procedure for the Langtry–Menter transition model combined with the SA turbulence model. They use a Newton–Krylov (NK) solver to this end and indicate good convergence behavior. Mosahebi and Laurendau [20, 21] used a modified decoupled approach to solve turbulence models that include transport equations for transition prediction. This approach also leads to favorable numerical behavior.

In this paper, we propose a smooth variation of the AFT model, referred to as AFT-S. The AFT-S model replaces discontinuous functions that feed the original AFT model's source terms by continuous surrogates. This makes the AFT-S model compatible with gradient-based aerodynamic shape optimization. We show that the smooth AFT-S model is able to recover the original AFT model's ability to predict transitional flows for which transition is triggered by the amplification of Tollmien–Schlichting (TS) waves. We modify and use an approximate Newton–Krylov (ANK) [22] solver to solve airfoil transitional flow problems and investigate the AFT and AFT-S numerical behaviors in terms of convergence and computational cost. We focus on airfoil cases for which the amplification of Tollmien–Schlichting (TS) waves triggers transition and present a three-dimensional test case that illustrates the AFT-S model applicability to realistic configurations. We assess the impact of distinct flow convergence levels on the transition front location and aerodynamic coefficients. We have used the AFT-S model to perform adjoint-based aerodynamic shape optimization, allowing the optimizer to explore the role of laminar-turbulent transition in an optimization process. The results can be found in our previous work [23].

The remaining sections of this paper are organized as follows. Section 2 introduces the AFT model, while Sec. 2.1 presents the AFT-S model variant. We provide information on our flow solver, ADFlow, in Sec. 3. The ANK solver is introduced in Sec. 3.1, which also contains information on modifications needed in the original solver to compute transitional flows using the AFT-S and AFT models. We present transitional flow results in Sec. 4 and highlight the AFT-S and AFT numerical behaviors and convergence characteristics in Sec. 5. We conclude with final remarks in Sec. 6.

2 Transport Equations for TS Wave Amplification

The AFT model was first proposed by Coder and Maughmer [12]. The original model was modified so that no isentropic flow assumption was needed and that Galilean invariance was achieved [24]. In a second version [25], the transport equation for the modified intermittency, $\tilde{\gamma} = \ln(\gamma)$, was introduced to improve robustness when complex flows are considered. A modified intermittency function is used so that the model can be implemented with different solver strategies, including finite element methods. Finally, after modifying some of the correlations that feed the transport equations, a new version was released [15]. The AFT model is briefly summarized in this section. For more information, please refer to Ref. [15].

The transport equations for the approximate N-factor, $\tilde{n}$, and modified intermittency, $\tilde{\gamma}$, are,

$$\frac{\partial(\rho\tilde{n})}{\partial t} + \frac{\partial(\rho u_j \tilde{n})}{\partial x_j} = \rho\Omega F_{\text{growth}} F_{\text{crit}} \frac{d\tilde{n}}{dRe_\theta} + \frac{\partial}{\partial x_j}\left[\sigma_n \left(\mu + \mu_t\right) \frac{\partial \tilde{n}}{\partial x_j}\right], \tag{2}$$

$$\begin{aligned}\frac{\partial(\rho\tilde{\gamma})}{\partial t} + \frac{\partial(\rho u_j \tilde{\gamma})}{\partial x_j} &= c_1 \rho S F_{\text{onset}} \left[1 - \exp(\tilde{\gamma})\right] - c_2 \rho \Omega F_{\text{turb}} \left[c_3 \exp(\tilde{\gamma}) - 1\right] \\ &+ \frac{\partial}{\partial x_j}\left[\left(\mu + \frac{\mu_t}{\sigma_\gamma}\right) \frac{\partial \tilde{\gamma}}{\partial x_j}\right],\end{aligned} \tag{3}$$

where ρ is the density, Ω is the vorticity magnitude, μ is the molecular dynamic viscosity, μ_t represents the eddy viscosity, and $\sigma_n = 1$ is a model constant. The modified intermittency, $\tilde{\gamma}$, relates to the intermittency through the mapping $\tilde{\gamma} = \ln(\gamma)$. For the modified intermittency transport equation, the model constants are $c_1 = 100$, $c_2 = 0.06$, $c_3 = 50$, and $\sigma_\gamma = 1.0$. The boundary conditions for both AFT working variables are homogeneous Dirichlet in the freestream and homogeneous Neumann on solid walls.

A complete description of source and diffusion terms in Eq. (2) and Eq. (3) is available in Ref. [15]. Below, we reproduce functions that are replaced by continuous surrogates in the AFT-S model variant, for which more details are provided in Sec. 2.1. Coder [15] proposes the use of a local shape factor, H_L, that is only based on variables available in each cell,

$$H_L = \frac{d^2}{\mu}\left[\vec{\nabla}(\rho\vec{u}\cdot\vec{\nabla}d)\cdot\vec{\nabla}d\right], \tag{4}$$

where d is the distance from the wall. The mapping between H_L and H_{12}, the boundary layer shape factor, is given by

$$H_{12} = \min\left[\max(0.26H_L + 2.4, 2.2), 20.0\right]. \tag{5}$$

The switching function in Eq. (2) reads

$$F_{\text{crit}} = \begin{cases} 0, & \text{if } \; Re_v < Re_{v,0}, \\ 1, & \text{if } \; Re_v \geq Re_{v,0}. \end{cases} \tag{6}$$

More details on the definitions behind Eq. (6) are available in Ref. [15]. The transition onset function is given by,

$$F_{\text{onset}} = \max[(F_{\text{onset},2} - F_{\text{onset},3}), 0], \tag{7}$$

$$F_{\text{onset},1} = \frac{\tilde{n}}{N_{\text{crit}}}, \tag{8}$$

$$F_{\text{onset},2} = \min\left(F_{\text{onset},1}, 2\right), \tag{9}$$

$$F_{\text{onset},3} = \max\left[1 - \left(\frac{R_T}{3.5}\right)^3, 0\right], \tag{10}$$

The the turbulent Reynolds number, R_T, is defined in Ref. [15]. In Eq. (8), N_{crit} is the critical N-factor, the threshold amplification that, when reached, indicates the beginning of the transition process. More details on the critical N-factor can be found in Refs. [15, 26].

The underlying SA turbulence model [14] reads,

$$\begin{aligned}\frac{D\tilde{\nu}}{Dt} = {} & c_{b1}S\tilde{\nu}\left(1 - f_{t2}\right) - \left(c_{w1}f_w - \frac{c_{b1}}{\kappa^2}f_{t2}\right)\left(\frac{\tilde{\nu}}{d}\right)^2 \\ & + \frac{1}{\sigma}\left\{\frac{\partial}{\partial x_j}\left[(\nu + \tilde{\nu})\frac{\partial\tilde{\nu}}{\partial x_j}\right] + c_{b2}\frac{\partial\tilde{\nu}}{\partial x_j}\frac{\partial\tilde{\nu}}{\partial x_j}\right\},\end{aligned} \tag{11}$$

and the coupling between the transition and turbulence transport equations takes place through a modification in the original f_{t2} function, which becomes

$$f_{t2} = c_{t3}\left[1 - \exp(\tilde{\gamma})\right]. \tag{12}$$

Spalart and Allmaras [14] describe the other variables in Eqs. (11) in more detail.

2.1 AFT-S

To be compatible with adjoint-based design optimization, a RANS model should preferably not include functions with discontinuous values or derivatives. The original AFT model contains min / max functions, which have discontinuous first derivatives, and switching step functions, which have discontinuous values. We propose a modified AFT model that uses smooth surrogates for discontinuous functions. The resulting smooth AFT model, called AFT-S, is used to obtain all of the flow results in this work that include transition to turbulence effects. The AFT-S model is based on the 2019b version of the original AFT model, for which additional details can be found in the literature [15].

The step function is used in the F_{crit} function in Eq. (6). We smooth this step function by using a modified hyperbolic tangent. The resulting function reads,

$$F_{\text{crit}} = \frac{1}{2}\left[1 + \tanh\left(\frac{Re_v - Re_{v,0}}{f_{\text{smooth}}}\right)\right], \tag{13}$$

where f_{smooth} is a constant set to 300 in the current implementation. This value was selected based on numerical experimentation and represents a good compromise between the desired function smoothing and the original AFT model's ability to recover the transition physics. Increasing values of f_{smooth} lead to a smoother function. To illustrate the smooth F_{crit} function, a $Re_{v,0}$ value of 3500 is used in Fig. 1.

The min and max functions are made smooth by using the Kreisselmeier–Steinhauser (KS) function [27], which has been used for constraint aggregation in structural optimization [28–30]. The KS function-based smoothing modification affects the H_{12}, F_{onset}, $F_{\text{onset},1}$, $F_{\text{onset},2}$, and $F_{\text{onset},3}$ computations. The maximum of generic functions F_1 and F_2 in a given computational cell is computed using a KS function as follows,

$$\max\left(F_1, F_2\right) = \frac{\ln\left[\exp\left(p_{\max} F_1\right) + \exp\left(p_{\max} F_2\right)\right]}{p_{\max}}, \tag{14}$$

where ln is the natural logarithm and $p_{\max}$ is a positive constant set to 100 in the current implementation. Equivalently, the minimum of functions F_1 and F_2 is computed by,

$$\min\left(F_1, F_2\right) = \frac{\ln\left[\exp\left(p_{\min} F_1\right) + \exp\left(p_{\min} F_2\right)\right]}{p_{\min}}, \tag{15}$$

where $p_{\min}$ is a negative constant, chosen to be equal to -100 in our current implementation. The current $p_{\max}$ and $p_{\min}$ values were chosen based on numerical experimentation with the goals of attenuating high-frequency oscillations in the residuals during the early convergence stages and of minimizing the number of nonlinear iterations needed to obtain accurate transition front location and drag coefficient estimates. As

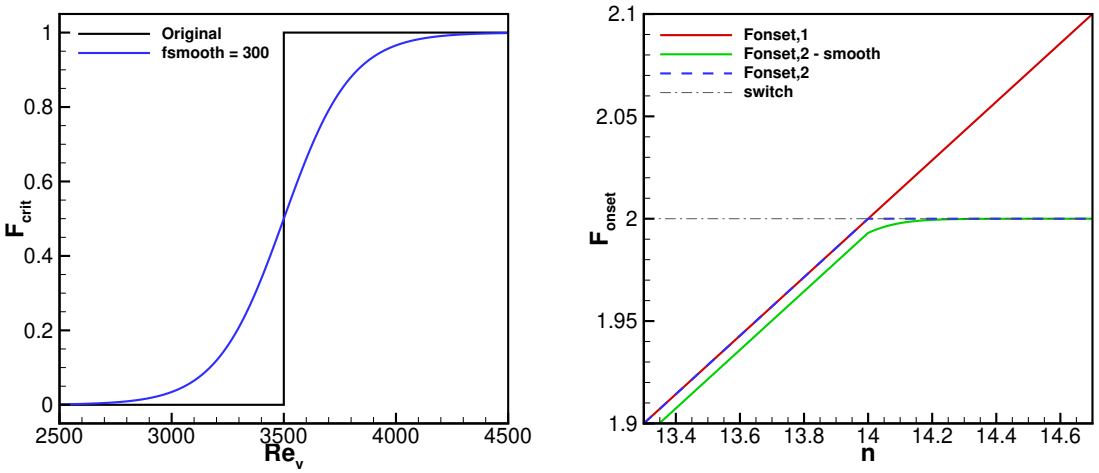

(a) F_{crit} (b) $F_{\text{onset},2}$, zoom-in.

Figure 1: Original and smooth F_{crit} and $F_{\text{onset},2}$ functions.

an example, the smooth version of $F_{\text{onset},2}$, originally defined in Eq. (9), is calculated as,

$$F_{\text{onset},2,\text{smooth}} = \frac{\ln\left[\exp\left(p_{\min} F_{\text{onset},1}\right) + \exp\left(2p_{\min}\right)\right]}{p_{\min}}. \tag{16}$$

The smooth version of $F_{\text{onset},2}$ is shown in Fig. 1 for $N_{\text{crit}} = 7$ and $p_{\min} = -100$. The image depicts the smooth version behavior in the neighborhood of the discontinuity region. The relevance of using the smooth version of the AFT model in gradient-based optimization is explained by the fact that step or min/max functions have undefined derivatives at their breakpoints.

3 CFD solver

We use ADflow to perform the simulations that generate the results in this paper. ADflow is an open-source CFD solver that can solve Euler, laminar Navier–Stokes, and RANS equations in steady, unsteady, and time-spectral modes, with multiblock structured and overset meshes [31]. The inviscid fluxes are discretized by using three different numerical schemes: the scalar Jameson–Schmidt–Turkel (JST) [32] artificial dissipation scheme, a matrix dissipation scheme based on the work of Turkel and Vatsa [33], and a monotone upstream-centered scheme for conservation laws (MUSCL) based on the work of van Leer [34] and Roe [35]. The viscous flux gradients are calculated by using the Green–Gauss approach. The residual equations can be converged with four distinct algorithms. Runge–Kutta and diagonalized-diagonally-dominant alternating direction implicit (D3ADI) [36] algorithms are available. An approximate Newton–Krylov (ANK) [22] solver is also implemented and can be used as a globalization scheme for the full Newton–Krylov (NK) solver [37]. Due to its robustness and numerical behavior, we adopt the ANK solver in this work.

3.1 Approximate Newton–Krylov Solver

We use an ANK algorithm to advance the flow state vector. The term approximate in the ANK algorithm refers to how simplified stencils are used in the Jacobian construction for the Newton step. When using the JST and Green-Gauss approaches to compute the inviscid and viscous fluxes on a structured grid, respectively, a 33-point stencil is needed for a second-order accurate finite volume formulation. We call this residual computation level $\mathcal{R}_0$. In a first approximation level, referred to as $\mathcal{R}_1$, we omit the fourth-order dissipation fluxes that are part of the JST scheme. This results in a 27-point stencil. In the higher approximation level, $\mathcal{R}_2$, we assume that the computational grid is perfectly orthogonal. The ANK solver was successfully applied to three-dimensional configurations using overset meshes, and the perfectly orthogonal grid assumption did not cause issues. Some examples can be found in Refs. [22, 38]. The stencils used for the turbulence equations are always compatible with the $\mathcal{R}_2$ approximation level [22]. The approximation introduced in $\mathcal{R}_1$ is also used in $\mathcal{R}_2$. This highest approximation level uses a 7-point stencil. These approximate routines are only used in the Jacobian computation and do not affect the actual set of equations solved. As a result, these approximations do not introduce any numerical errors in the final solution because they only affect the converged state's path and not the converged state itself. Further details on the approximations involved in our ANK algorithm are provided by Yildirim et al. [22].

In CFD simulations, the initial solution is generally based on the constant, freestream state, and therefore, continuation strategies are necessary [39]. In a pseudo-transient continuation (PTC) approach, artificial time dependence is added to the steady-state problem to make the state follow a physically valid trajectory from the initial condition to the final state [39]. The ANK algorithm advances the state vector, $\mathcal{Q}$, by using a

PTC strategy, according to

$$\left(\frac{\mathcal{I}}{\Delta t^{(n)}} + \left(\frac{\partial \mathcal{R}_m}{\partial \mathcal{Q}}\right)^{(n)}\right) \Delta \mathcal{Q}^{(n)} = -\mathcal{R}_0\left(\mathcal{Q}^{(n)}\right), \tag{17}$$

where $\mathcal{I}$ is the identity matrix, $\mathcal{R}$ represents the residual equations, the subscript m indicates the residual approximation level, and superscripts denote the values evaluated at the n^{th} iteration. The iteration process aims at defining a state vector that respects $\mathcal{R}_0 = \mathbf{0}$. The turbulence system, which can be solved in coupled or decoupled manner, uses a first-order accurate upwind scheme for the advection terms. In the approximate levels, the production term for the SA model, as defined in Eq. (11), is omitted for fully turbulent simulations using the original SA model. When the AFT or AFT-S models are used, the production term in the underlying SA model is retained since the coupling between turbulence and transition transport equations takes place through the f_{t2} term, as defined in Eq. (12). The omission of the SA model production term favors the numerical convergence during the stages in which the approximate residual levels are used [22]. In the AFT and AFT-S models, production and destruction terms are combined under a single term for the approximate N-factor transport equation, as seen in Eq. (2). For the modified intermittency transport equation, defined in Eq. (3), production and destruction are represented by two separate terms. Therefore, omitting the production term was not possible in the modified N-factor equation. Numerical experimentation did not indicate benefits in omitting the production term in the modified intermittency transport equation combined with the residual level approximations. Yildirim et al. [22] provide a complete description of the stencils used in our implementation.

For each nonlinear iteration, the state vector is updated following,

$$\mathcal{Q}^{(n+1)} = \mathcal{Q}^{(n)} + \omega^{(n)} \Delta \mathcal{Q}^{(n)}, \tag{18}$$

where $\omega^{(n)}$ is a relaxation factor with a value between 0 and 1. To determine $\omega^{(n)}$, we first compute ω_{phys}, which is used to limit the updates so that the states respect predetermined physical bounds,

$$\omega_{\text{phys}} = \left[\max\left(\left\{\left|\frac{\Delta \mathcal{Q}_{i,l}}{\lambda_{\text{phys},l}\mathcal{Q}_{i,l}}\right| ; \forall\ \left(i \in n_{\text{cell}}\right), \left(l \in l_{\text{phys}}\right)\right\}, 1\right)\right]^{-1}, \tag{19}$$

where the subscripts i and l refer to the cell index and the variable index respectively, n_{cell} is the global cell count, and l_{phys} represents the variable indices subject to the physicality check. For the meanflow equations, we use $\lambda_{\text{phys},\rho} = \lambda_{\text{phys},E} = 0.2$, where the subscripts ρ and E indicate density and energy, respectively. For the SA working variable, $\tilde{\nu}$, we use $\lambda_{\text{phys},\tilde{\nu}} = 0.99$. This allows the solver to increase $\tilde{\nu}$ rapidly if needed.

Modifications to the original physicality check are required to simulate transitional flows. When solving for the AFT and AFT-S additional states, $\tilde{n}$ and $\tilde{\gamma}$, we proceed as follows. Numerical experimentation indicated that control over the approximate N-factor, $\tilde{n}$, is unnecessary. The modified intermittency, $\tilde{\gamma}$, is not allowed to assume values larger than 2. For this variable, we use $\lambda_{\text{phys},\tilde{\gamma}} = 1.0$. The steps used to determine ω_{phys}

Algorithm 1 Physicality check

$\omega_{\text{local}} \leftarrow 1$ ▷ Initialize the local step to 1
for i **in** $n_{\text{cells,local}}$ **do** ▷ Loop over every cell owned by this process
  for l **in** $[l_\rho, l_E]$ **do** ▷ Loop over density and energy variables
    $\omega_{\text{local}} \leftarrow \left[\max\left(\left|\frac{\Delta\mathcal{Q}_{i,l}}{\lambda_{\text{phys},l}\mathcal{Q}_{i,l}}\right|, \frac{1}{\omega_{\text{local}}}\right)\right]^{-1}$ ▷ Limit the step such that $|\Delta\mathcal{Q}_{i,l} < \lambda_{\text{phys},l}\mathcal{Q}_{i,l}|$
  for $l = l_{\tilde{\nu}}$ **do** ▷ Check the SA model working variable
    if $\Delta\mathcal{Q}_{i,l} < 0$ **then** ▷ Only check negative updates
      $\omega_{\text{local}} \leftarrow \left[\max\left(\left|\frac{\Delta\mathcal{Q}_{i,l}}{\lambda_{\text{phys},l}\mathcal{Q}_{i,l}}\right|, \frac{1}{\omega_{\text{local}}}\right)\right]^{-1}$ ▷ Limit the step so that $|\Delta\mathcal{Q}_{i,l} < \lambda_{\text{phys},l}\mathcal{Q}_{i,l}|$
  for $l = l_{\tilde{\gamma}}$ **do** ▷ Check the modified intermittency
    if $\mathcal{Q}_{i,l} \neq 0$ **then** ▷ Check for nonzero states
      $\omega_{\text{local}} \leftarrow 1$
      if $\mathcal{Q}_{i,l} + \Delta\mathcal{Q}_{i,l} > 2$ **then** ▷ Check if update violates $\tilde{\gamma}$ bound
        $\omega_{\text{local}} \leftarrow \left|\frac{\left(\Delta\mathcal{Q}_{i,l}-2\right)}{\Delta\mathcal{Q}_{i,l}}\right|$ ▷ Limit the step so that $|\Delta\mathcal{Q}_{i,l} < \lambda_{\text{phys},l}\mathcal{Q}_{i,l}|$
    else ▷ Check for zero states
      if $\Delta\mathcal{Q}_{i,l} > 2$ **then**
        $\omega_{\text{local}} \leftarrow \left|\frac{-2}{\Delta\mathcal{Q}_{i,l}}\right|$ ▷ Limit the step so that $|\Delta\mathcal{Q}_{i,l} < \lambda_{\text{phys},l}\mathcal{Q}_{i,l}|$
      else
        $\omega_{\text{local}} \leftarrow 1$ ▷ Take a full step
    if $\omega < \omega_{\min,\tilde{\gamma}}$ **then** ▷ Check if step is too restrictive
      $\omega_{\text{local}} \leftarrow 1$ ▷ Take a full step
      if $\mathcal{Q}_{i,l} + \Delta\mathcal{Q}_{i,l} > 2$ **then**
        $\Delta\mathcal{Q}_{i,l} = \mathcal{Q}_{i,l} - 2$ ▷ If full step violates upper bound, clip the update
$\omega_{\text{phys}} \leftarrow \text{MPI\_Allreduce}(\omega_{\text{local}}, \min)$ ▷ Communicate to determine the global minimum ω_{local}

are listed in Algorithm 1. Unlike the SA working variable, the modified intermittency is allowed to assume negative and positive values. This makes necessary the modification of the physicality check. If, in a given cell, the modified intermittency is nonzero, we set $\omega_{\text{local}} = 1$, allowing a full step. If the full step leads to $\tilde{\gamma} > 2$, we limit the step to avoid the modified intermittency growing beyond the upper limit. If the modified intermittency is zero for a given cell, we check the update and, if it is larger than the upper bound for this state, we limit the local step accordingly. If this violation does not occur, a full step is used. In the physicality check for the modified intermittency, we set a lower limit of $\omega_{\text{min},\tilde{\gamma}} = 0.05$. If ω_{phys} assumes this lower bound value at a given cell, we allow a full unit step and check if this violates the upper bound for the modified intermittency. If an upper bound violation occurs, the state update is clipped. After the physicality check, we employ a backtracking line search to determine the maximum step size that leads to a decrease in the unsteady residual norm [22].

4 Numerical Results

This section presents numerical results obtained with the AFT-S transition model for two subsonic airfoil test cases for which experimental data with transition information are available. For the NLF(1)-0416 airfoil, which is a standard transition prediction test case for which a complete set of experimental data is available, we compare the results obtained with the AFT-S model with those corresponding to the original AFT model. We highlight the AFT-S capability to predict the correct transition onset location and illustrate its positive impact on the drag polar computation. A three-dimensional case based on the prolate spheroid geometry is also presented. For all test cases used here, a freestream eddy viscosity ratio of 2.79×10^{-7} was used, following Ref.[15]. This value directly maps to $\tilde{\nu}/\nu = 0.1$.

4.1 NACA 0012

Gregory and O'Reilly [40] obtained experimental transition locations for a NACA 0012 airfoil. The wind tunnel runs had a Reynolds number of 2.88×10^6 and a Mach number of 0.16. No information on the turbulence level on the wind tunnel test section is available. Using an e^N method and varying the turbulence intensity to produce the best transition point match at a zero angle of attack, Mosahebi and Laurendeau [21] suggested a freestream turbulence intensity, Tu, of 0.5% for a Mach number of 0.1. We select freestream turbulence intensities of 0.2%, 0.4%, and 0.5% for the present computations with angles of attack of 0, 3, 5, and 8 degrees. The computational mesh has 116,760 cells with a y^+ value no larger than 0.28. The mesh is composed of 805 grid points in the streamwise direction, with around 50 points inside the boundary layer region. The mesh growth ratio in the wall-normal direction is 1.05. The meshes used in this study follow the guidelines suggested by Coder [41]. Grid convergence studies indicate that the present mesh leads to the expected numerical behavior. The mesh is similar to the fine airfoil mesh described by Coder [41].

Transition locations for all angles of attack and turbulence intensities used are shown in Fig. 2. These results indicate that a turbulence intensity of 0.5% leads to

the best agreement with experimental data. Therefore, despite the slight differences in Mach number between the experimental setup [40] and the e^N results [21], the estimated wind tunnel test section is a good value to be used with the AFT-S transition model. Figure 2 also shows the transition front evolution for a zero angle of attack for varying turbulence intensity levels. As expected, increasing turbulence values move the transition front upstream. Previous investigations assessed the Langtry–Menter (LM) model's ability to capture the effects of varying turbulence intensities on the transition front [42]. These investigations recommended good practices for specifying freestream turbulence variables when using the LM model with typical aeronautical configurations [3, 17]. Future investigations will further explore these aspects when considering the AFT-S model. In this work, the transition location is defined as the

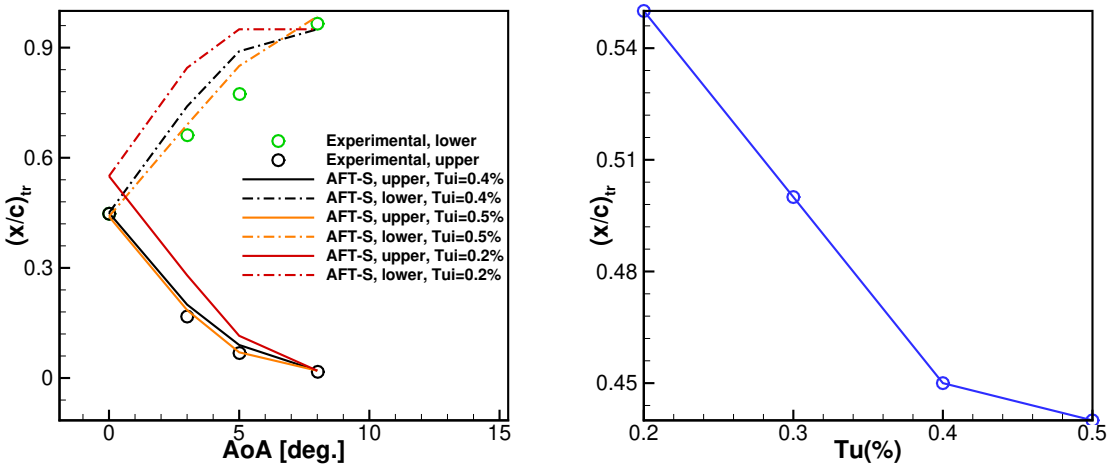

(a) Lower and upper transition locations

(b) Tu effect, zero angle of attack

Figure 2: Transition location variations with angle of attack and turbulence intensity for the NACA 0012 airfoil.

chordwise position where the skin friction coefficient first rises following the laminar flow region. As pointed out by Arnal [43], the maxima of quantities such as skin friction coefficient, RMS voltage, and wall heat flux are often used as an indication of transition location. However, these peak values correspond to the middle of the transition region, with an intermittency factor of around 0.5. The skin friction and pressure coefficients for a zero angle of attack and $Tu = 0.5\%$ are shown in Fig. 3. This corresponds to a critical amplification factor of $N_{\text{crit}} = 4.29$. The skin friction coefficient moves up at $x/c = 0.425$, defining the transition onset point. We observe a small perturbation in the pressure coefficient distribution at this same location, indicating the transition region. In aerodynamic flows that do not present shock waves, the effect of transition on the pressure coefficient distribution is only of second order.

Approximate amplification factor, $\tilde{n}$, and modified intermittency, $\tilde{\gamma}$, are shown in Fig. 4. We zoom in around the transition location indicated by the c_f distribution, seen in Fig. 3. In the transitional region, the approximate N-factor overcomes the critical value, $N_{\text{crit}} = 4.29$, which triggers the activation of the turbulence terms in

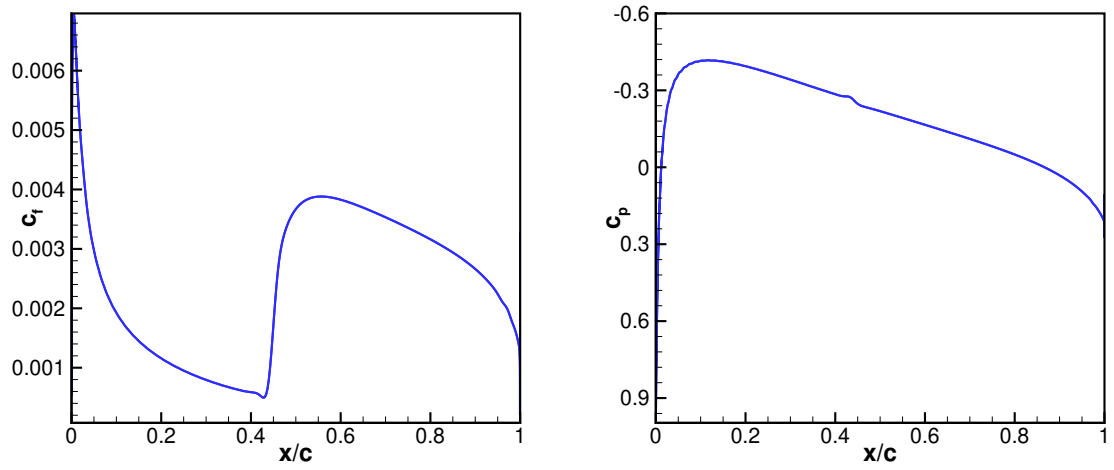

(a) Skin friction coefficient

(b) Pressure coefficient

Figure 3: Skin friction and pressure coefficients for a zero angle of attack and $Tu = 0.5\%$ for the NACA 0012 airfoil.

the SA model transport equation. Modified intermittency contours in yellow indicate turbulent flow, while purple denotes laminar. In the AFT-S model, both approximate amplification factor, $\tilde{n}$, and modified intermittency assume a zero value at the farfield. Since the modified intermittency is the natural logarithm of the true intermittency, zero values of $\tilde{\gamma}$ indicate turbulent flow, and decreasing negative values indicate laminar flow. Therefore, the modified intermittency field represents a turbulent state that turns laminar close to the wall ahead of the transition zone. In Fig. 4, velocity profiles are superimposed on the transition transport equations states contours. One can see that the velocity profiles initially represent laminar flow and subsequently become full, indicating a turbulent flow state.

4.2 NLF(1)-0416

The general aviation NLF(1)-0416 airfoil is a relevant test case for transitional flow analysis due to the availability of experimental data with free transition. For the simulations presented here, the Reynolds number is 4×10^6, and the Mach number is fixed at 0.1. Following the suggestions by Coder [41], we use a freestream turbulence intensity of $Tu = 0.15\%$, corresponding to $N_{\text{crit}} = 7.17$. The computational mesh has 304,000 cells and respects the leading and trailing edges spacings and off-wall spacing suggested by Coder [41]. The mesh is composed of 1000 grid points in the streamwise direction, with approximately 304 points in the wall-normal direction. This leads to a y^+ no greater than 0.65. The mesh growth rate in the wall-normal direction is lower than 1.1. The farfield boundaries are placed at 1000 chords away from the airfoil surface following Ref. [41].

We perform simulations considering angles of attack from -4 to 8 degrees, with increments of 2 degrees, and compare the numerical results to experimental data from

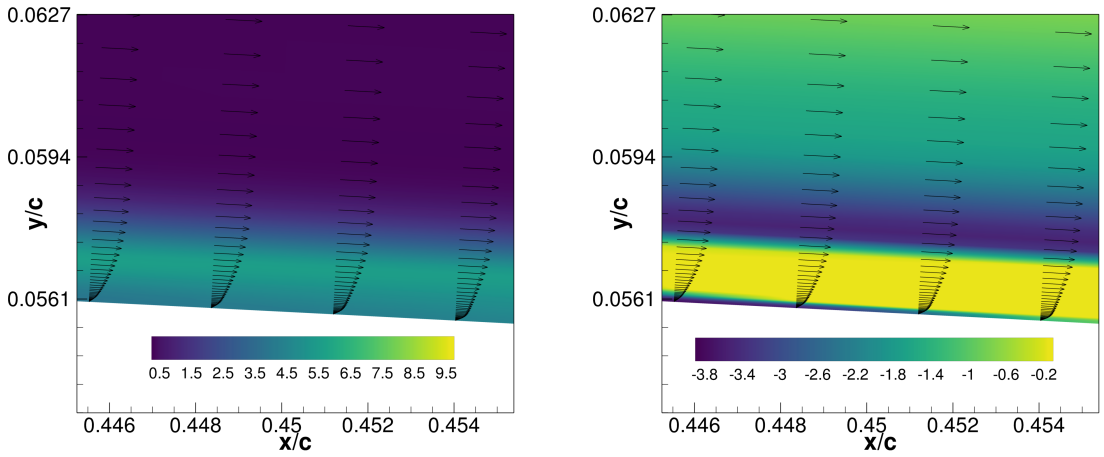

(a) Approximate N-factor

(b) Modified intermittency

Figure 4: $\tilde{n}$ and $\tilde{\gamma}$ contours for zero angle of attack and $Tu = 0.5\%$ for the NACA 0012 airfoil. Velocity profiles are superimposed.

Somers [44]. Transition front locations and drag polar results for both transitional (AFT and AFT-S) and fully turbulent (SA) cases are shown in Fig. 5. The experimental transition locations reported by Somers [44] are obtained through the use of acoustic devices that do not precisely detect transition. Instead, this method suggests bounds inside which transition takes place. In Fig. 5, the triangular symbols connected by horizontal bars indicate the likely transition locus for each lift coefficient. With increasing angles of attack, the suction peak becomes more pronounced, and the resulting increasingly strong adverse pressure gradients amplify TS waves, moving the transition front upstream in the airfoil suction side. On the pressure side, the accelerating flow caused by the increasing angles of attack has a damping effect on the TS waves, moving the transition front downstream. The AFT-S model correctly reproduces this behavior. Inspection of Fig. 5 also indicates that the transition locations predicted by the AFT-S model are similar to the ones obtained using the original AFT model. The drag polar results on the right of Fig. 5 demonstrate that including transition to turbulence effects improves agreement with experimental data. We observe that the drag polar results for the NLF(1)-0416 airfoil obtained with the AFT-S model compare well to those obtained with the original AFT model. Additional results for the NLF(1)-0416 airfoil using the original AFT model can be found in Refs. [15, 18, 45].

Pressure coefficient distributions for experimental, transitional, and fully turbulent simulations are shown in Fig. 6. Since this is a subsonic test case, the inclusion of transition does not significantly affect the pressure distribution, with good agreement with experimental data for both transitional and fully turbulent cases. However, one can observe that the pressure coefficient region corresponding to the transition location on the suction side of the airfoil presents a slope variation that is only captured when the numerical results include transition to turbulence effects. The results shown in Fig. 6 also indicate that the AFT-S model computation leads to a pressure coefficient

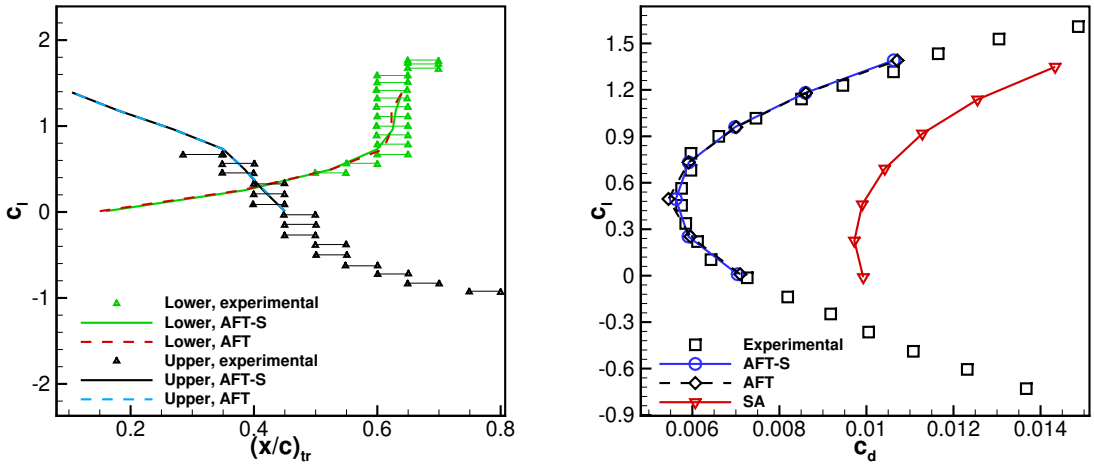

(a) Transition locations (b) Drag polar

Figure 5: Transition locations and drag polar for the NLF(1)-0416 airfoil.

distribution that is indistinguishable from the one obtained with the original AFT model. All AFT simulations presented here are based on the 2019b version, for which details are presented in Ref. [15]. We recall that the AFT-S model is constructed on top of this same AFT model version.

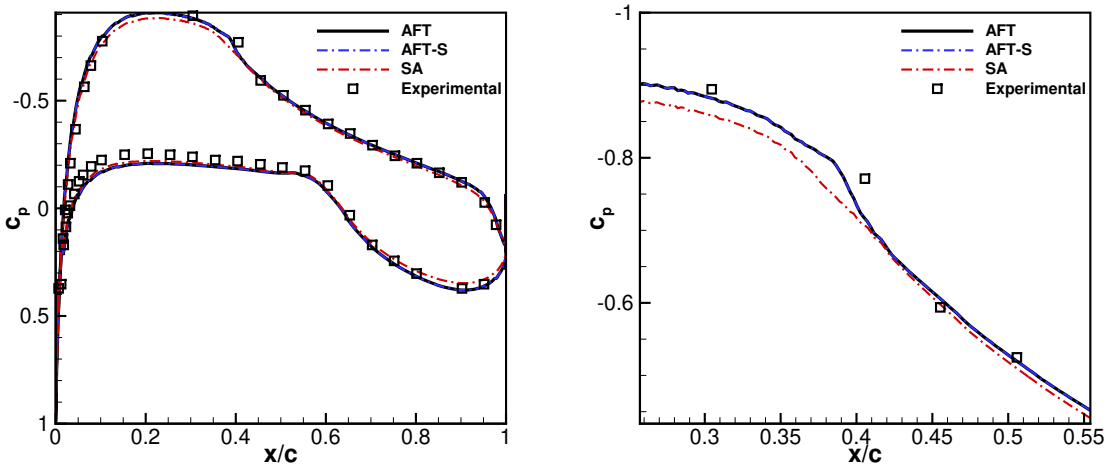

(a) c_p, overview (b) c_p, zoom-in around the transition region

Figure 6: Pressure coefficient distributions for a zero angle of attack case for the NLF(1)-0416 airfoil.

Skin friction coefficient results for both transitional (AFT and AFT-S) and fully turbulent (SA) cases are shown in Fig. 7. The transitional case presents the typical skin friction coefficient behavior observed in transitional flow, where a rapid increase of c_f indicates the transition onset point, as was mentioned in Sec. 4.1. The fully turbulent case presents higher skin friction coefficients for both suction and pressure

sides of the airfoil. This is a result of the boundary layer starting turbulent when the SA model is used. Skin friction coefficient evolutions also indicate that the AFT-S model correctly retains the behavior of the original AFT model. The transition locations are the same for the AFT-S model and the original AFT model, as shown by the skin friction coefficient rises seen in Fig. 7. Details on the lift and drag coefficient comparisons between AFT-S and AFT results are presented in Sec. 5.

In the transitional case, the fully turbulent boundary layer is affected by the previous laminar and transitional states throughout history effects caused by the boundary layer's convective nature. This explains the distinct c_f distributions for the post-transitional, turbulent boundary layer in the simulations using the AFT-S model and the turbulent boundary layer obtained with the SA model. Similar results were observed when using a flow stability module based on the parabolized stability equations coupled to a high-order CFD code [2]. For subsonic flow at low angles of attack, only small, if any, flow separation regions appear, and the drag is dominated by skin friction. This is the main reason why the fully turbulent cases produce a drag polar that is visibly different from the experimental one, as observed in Fig. 5.

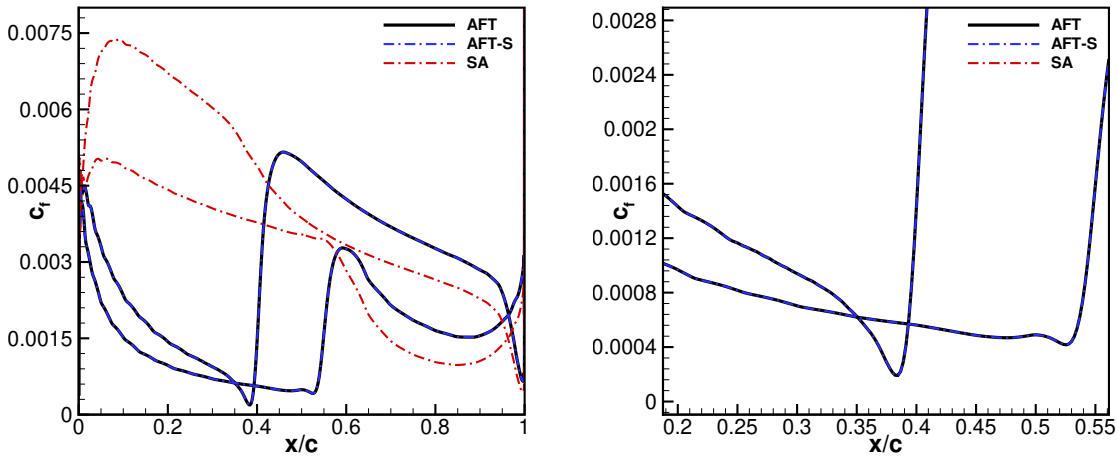

(a) c_f, overview

(b) c_f, zoom-in around the transition region

Figure 7: Skin friction coefficient distributions for a zero angle of attack case for the NLF(1)-0416 airfoil.

Approximate N-factor, $\tilde{n}$, and modified intermittency, $\tilde{\gamma}$, contours are shown in Fig. 8 for the AFT-S model. The zoomed-in images correspond to the transition location in the suction side of the airfoil for a zero angle of attack, seen in Fig. 7. Velocity profiles indicating laminar and transitional boundary layers are also shown. For a freestream turbulence intensity of $Tu = 0.15\%$, the corresponding $N_{\text{crit}} = 7.17$ is exceeded in the transitional boundary layer. The modified intermittency contours also indicate the presence of a transition zone around $x/c = 0.385$, which agrees with the skin friction distribution shown in Fig. 7.

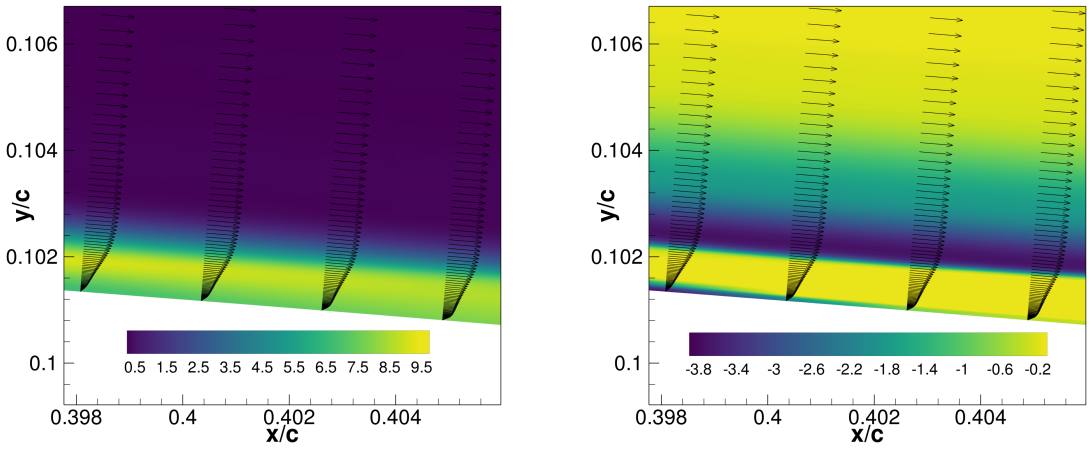

(a) Approximate N-factor

(b) Modified intermittency

Figure 8: $\tilde{n}$ and $\tilde{\gamma}$ contours for a zero angle of attack for the NLF(1)-0416 airfoil. Velocity profiles are superimposed.

4.3 Inclined 6:1 Prolate Spheroid

The inclined prolate spheroid is a test case that embeds flow phenomena typical of a fuselage. This test case represents a challenge for correlation-based transition models because fuselage-like configurations are not present in the experimental data that were used to derive the correlations. Kreplin et al. [46] performed experimental measurements in the DFVLR 3x3 low-speed wind tunnel facility in Göttingen, Germany. The experimental data was obtained for Mach numbers of $M = 0.03$ and $M = 0.136$, with Reynolds numbers of $Re = 1.5 \times 10^6$ and $Re = 6.5 \times 10^6$. The angle of attack was set to 5, 10, and 15 degrees. For $Re = 1.5 \times 10^6$ and $M = 0.03$, transition to turbulence was triggered by amplification of TS waves. For $Re = 6.5 \times 10^6$ and $M = 0.136$ with angles of attack of 5 and 10 degrees, transition is caused by both TS and crossflow modes being amplified in the boundary layer. When the higher Reynolds and Mach numbers are combined to an angle of attack of 15 degrees, transition to turbulence is dominated by crossflow instability modes. The current AFT-S implementation does not include empirical correlations for crossflow instabilities, and we choose $M = 0.03$ and $Re = 1.5 \times 10^6$ with an angle of attack of 10 degrees as the flow condition for the numerical simulations. As mentioned earlier, transition is dominated by TS-wave amplification for these flow conditions. In the wind tunnel, the freestream turbulence intensity is reported to be around 0.10% for this case. Numerical results considering the Langtry-Menter transition model, for this same test case, are available in the work from Grabe and Krumbein [47].

For the simulations, we use a mesh with $4,194,304$ elements with corresponding y^+ values no larger than 0.3. Our computational mesh follows the guidelines suggested in Ref. [41]. Because ADflow is based on a compressible flow formulation, we perform our simulations considering $M = 0.1$ instead of $M = 0.03$. ADflow does not employ low Mach number preconditioning [48], and we have observed convergence issues at Mach

numbers lower than 0.1.

The AFT-S model successfully captures the transition front when TS-waves dominate the process. Skin-friction coefficient contours are seen in Fig. 9. The thick black line represents the transition front obtained experimentally. As one can see by inspecting the results shown in Fig. 9, the transition front predicted by the AFT-S model closely recovers the experimental behavior.

To investigate the freestream turbulence intensity, Tu_i, effect on the transition front, we also perform a simulation considering $Tu_i = 0.15\%$. The skin friction coefficient contours for this freestream condition are also shown in Fig. 9. When compared to the results corresponding to $Tu_i = 0.1\%$, the higher freestream turbulence intensity simulation only reveals minor differences in flow topology.

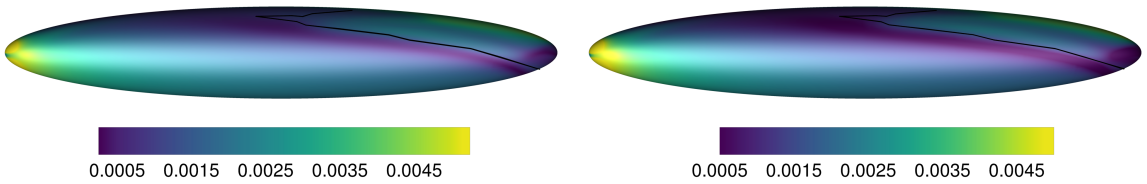

(a) $Tu_i = 0.10\%$ (b) $Tu_i = 0.15\%$

Figure 9: Skin friction coefficient contours for the prolate spheroid at a 10-degree angle of attack.

For this flow condition, a complex flow topology is observed. A flow separation regions extends throughout the prolate spheroid. Skin friction contours combined with shear lines are seen in Fig. 10. In this figure, the separation region is evidenced by the shear line convergence zone. This fuselage-like flow topology represents, as mentioned earlier, a challenge for correlation-based transition models.

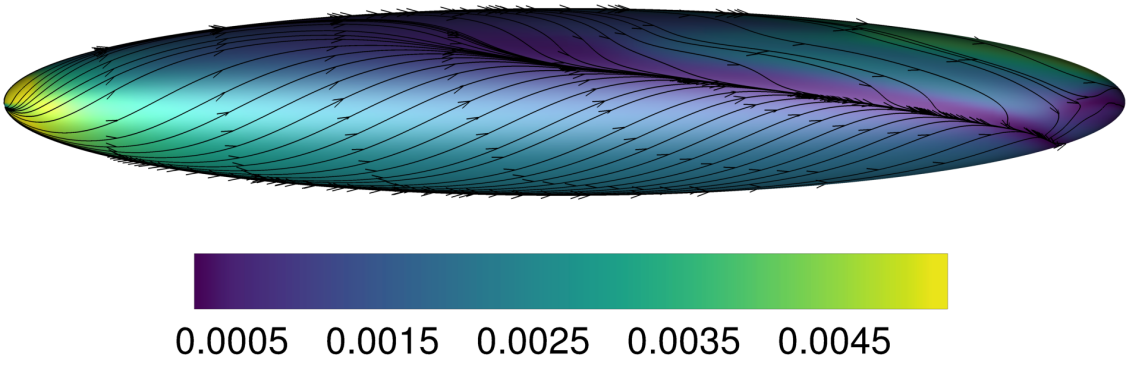

Figure 10: Skin friction coefficient contours with shear lines superimposed for the prolate spheroid at a 10-degree angle of attack.

The numerical results presented in this section indicate that the AFT-S model is

able to recover the original AFT model behavior. Our results also show that the AFT-S model is able to reproduce experimental transitional flow results for airfoil flow cases. Finally, the prolate spheroid results illustrate the ability of the AFT-S model to recover experimental results when transition is observed in complex, three-dimensional flow configurations for which TS-wave amplification is the leading transition mechanism.

5 Numerical Behavior and Convergence

The inclusion of turbulence equations in the set of meanflow equations dramatically increases the complexity of the nonlinear system since the turbulence variables present large fluctuations in the early convergence phases. The SA working variable is also 3 to 4 orders of magnitude smaller than the meanflow variables, requiring some type of scaling. Introducing the transport equations for transition variables further enhances the system complexity, directly impacting the numerical convergence behavior. The large number of discontinuous functions that feed the source terms present in the transition transport equation hinder the transition model convergence characteristics.

Based on the work of Lian et al. [49], Piotrowski and Zingg [19] propose a coupled solution procedure for the Langtry–Menter transition model combined with the SA turbulence model. Their approach combines a smooth version of the LM model with a source term time-stepping approach proposed by Lian et al. [49] and is based on an NK solver with approximate and inexact phases. The source term time-stepping approach uses the eigenvalues of the Jacobian formed by the turbulence and transition equations production terms. If the larger positive eigenvalue overcomes $0.9/\Delta t$ in a given cell, the local pseudo time step is reduced.

Mosahebi and Laurendau [20, 21] proposed a modified decoupled approach to solve turbulence models that include transport equations for transition prediction. Their solver uses a modified explicit five-step Runge–Kutta time scheme. They used this approach to converge the LM transition model robustly. In this modified decoupled approach, each transport equation is solved separately, leading to a scalar Jacobian. Furthermore, the coupling between the transition and turbulence equations, performed through an effective intermittency, γ_{eff}, is under-relaxed. This gradually introduces the effects of transition into the k and ω equations that form the SST model's turbulence system.

In ADflow, we use a decoupled approach to solve the flow problem with the ANK solver. The turbulence variables are updated following the meanflow variables updates in each nonlinear iteration in a nonlinear block Gauss–Seidel fashion [22]. By using this decoupled approach, we recover the favorable convergence characteristics observed in the meanflow variables. This also alleviates the difficulties associated with the scaling of variables that arises when a fully coupled approach is used. The decoupled approach improves the linear system conditioning and allows us to monitor the linear solver performance for the turbulence system alone. This allows us to only update the PC for the turbulence system while retaining a lagged PC for the meanflow variables [22]. In the NK solver, a fully-coupled approach is used. Previous studies [22] using the SA turbulence model have shown that decoupled simulations behaved better in terms

of wall time, and approximation levels $\mathcal{R}_2$ and $\mathcal{R}_1$ performed better than $\mathcal{R}_0$ in the decoupled approach. As mentioned in Sec. 3.1, the approximate routines lead to more nonlinear iterations and increase the diagonal dominance in the Jacobian, making each nonlinear iteration computationally less expensive. These investigations also indicated that a more robust method to choose the switching point between the ANK and NK phases is required. Coupled simulations stalled after a relative convergence of 5 orders of magnitude since the backtracking line search returned $\omega = \omega_{\min}$. To avoid this issue, we use the ANK solver only for the transitional flow analyses presented here.

To investigate the convergence behaviors for the original AFT model and for the smooth AFT-S model, we simulate the transitional flow over the NLF(1)-0416 airfoil at a zero angle of attack, M = 0.2 and Re = 4×10^6. We use the NLF(1)-0416 mesh considered in the validation study presented in Sec. 4.2 since that mesh was able to provide good agreement with experimental data and, therefore, the discussions below apply to simulations that recover the correct transitional flow physics. We choose $M = 0.2$ for the simulations that follow to reduce run-time because a converged state is reached faster for the higher Mach number. Since a validation against experimental data using $M = 0.1$ was performed in Sec. 4.2, we believe that the current choice for the Mach number is justifiable. Our ANK solver has many setup options, and we use two distinct flow strategies in this study. In the engineering convergence strategy, we solve the transitional flow problem by refreshing the turbulent PC every 10 iterations. We also allow one nonlinear iteration of the turbulence model variables during the decoupled solver and set the linear system tolerance to 0.05. Numerical experimentation also suggested a 10^4 scaling factor for the SA working variable residuals. For both the transitional variables, we use a residual scaling factor of 100. The CFL limit is set to 100. This is required to allow the initial laminar flow solution to develop before the transition to turbulence can start. In this simulation, we use the default residual formulation of the ANK solver. The solver details for the engineering convergence strategy are present in Table 1.

Table 1: Details for solver options - engineering and deep convergence strategies.

Variable	Engineering convergence	Deep convergence
Turbulence PC refreshing interval	10 iterations	1 iteration
Turbulence system sub-iterations	1	25
Linear system tolerance	0.05	10^{-4}
Residual scalings ($\tilde{\nu}$,$\tilde{n}$,$\tilde{\gamma}$)	(10^4,10^2,10^2)	(1.0,1.0,1.0)
CFL limit	100	1000
$\mathcal{R}_0$ switch	not used	10^{-4}

In the early nonlinear iterations, we observe a decay in the residuals for both AFT and AFT-S models. Residuals for the modified amplification factor, $\tilde{n}$, start at low values and then undergo a rise when wave amplification starts, even if the overall flow state is laminar. During this early stage, the laminar flow that precedes turbulence is developing. Suppose a convergence criterion is set to exit the simulation during this first deep residuals decay. In that case, the resulting flow field will be laminar

because the source terms in the SA turbulence model are not yet fully activated. The residuals rise following this initial decay. At this point, wave amplification in the trailing edge region becomes apparent. During the solution process, transition occurs at a location downstream of its final location and then moves upstream until it settles. For the engineering convergence strategy, this happens around 7000 nonlinear iterations for the AFT-S model, while in the original model, the transition front settles after 6000 nonlinear iterations. At this point, the flow solver is no longer able to reduce the residuals, and some high-frequency oscillations are observed for the AFT-S variant, but no bulk reduction takes place. When the original AFT model is used, the oscillations disappear after 6000 nonlinear iterations. In both cases, the aerodynamic coefficients are converged when the transition front settles. We use freestream residuals as a reference. A relative convergence is then defined as,

$$\eta_{\text{rel}}^{(n)} = \frac{||\mathcal{R}_0^{(n)}||_2}{||\mathcal{R}_0^{(\text{fs})}||_2}, \tag{20}$$

where the superscript fs refers to the freestream properties. The relative convergence for the governing equations is shown in Fig. 11. The convergence levels observed in this strategy are compatible with industry standards.

After the solution stalls and the transition front is settled, the engineering convergence strategy applied to the AFT-S model leads to a lift coefficient of $c_l = 0.5$ and a drag coefficient of $c_d = 0.005462$, which is in agreement with experimental data [44]. When the original AFT model is used, the engineering convergence strategy leads to a lift coefficient of $c_l = 0.4999$ and a drag coefficient of $c_d = 0.005474$. These values also represent good agreement with the experimental data and indicate that the AFT-S model can recover the original AFT model behavior. The drag coefficient is different by only 0.22% when comparing results from the AFT-S model with the original AFT. The lift and drag coefficient evolutions for the engineering convergence strategy are shown in Fig. 12 for the AFT-S model. In Fig. 12, we only display 6000 out of the 10000 nonlinear iterations used in the engineering convergence strategy since no visible variations in the force coefficients can be graphically seen past this point. As mentioned by Mavriplis et al. [50], the lift coefficient presents a slow convergence during the early iterations in Newton solvers, which is in agreement with the behavior seen in Fig. 12. During the final 5000 nonlinear iterations, during which high-frequency oscillations are observed in the residuals, the drag coefficient variations are within 0.1 drag count, or around 0.18%.

Results available in the literature trace the convergence stalling seen in 2-equation transition models to localized intermittency jumps in the viscous sublayer region [51]. This indicates that the modified intermittency equation is at least partially responsible for the convergence stalling. Mavriplis et al. [51] also suggest that these harmful low to high modified intermittency variations occur downstream of the transition region and that the modified intermittency can be frozen after the transition location is settled to remedy this issue. In our current implementation, the use of a frozen modified intermittency field did not help address the convergence stalling mentioned above. To further investigate the AFT and AFT-S convergence behaviors, we propose a second flow solver strategy, referred to as deep convergence strategy.

In the deep convergence strategy, we allow the turbulence subsystem to perform more iterations for each meanflow iteration. In this case, we perform 25 turbulence iterations for each meanflow iteration. We also enforce the preconditionner (PC) to be refreshed every iteration instead of every 10 iterations in the engineering convergence strategy. We tighten the linear system tolerance, which is reduced to 10^{-4}, and do not scale the turbulence variables. A CFL ramp with a maximum value of 1000 is used. The $\mathcal{R}_0$ approximation level, in which a 33-point stencil is needed for a second-order accurate finite volume formulation, is activated after total residuals present a relative convergence of 4 orders of magnitude. The setup used in the deep convergence strategy is shown in Table 1.

By using the deep convergence strategy, which promotes a better convergence for the turbulence subsystem, we obtain machine zero convergence after 2660 and 2515 nonlinear iterations when using AFT-S and AFT models, respectively. The convergence history is shown in Fig. 11. Using the deep convergence strategy, we obtain a lift coefficient of $c_l = 0.5$ and a drag coefficient of $c_d = 0.005459$ with the AFT-S model. As for the engineering convergence strategy, lift and drag coefficients initially present oscillations. After 600 nonlinear iterations, lift and drag coefficients present minor variations only, with drag coefficient variations within 0.1 drag count, for both AFT-S and AFT. When applied to the original AFT model, the deep convergence strategy leads to a lift coefficient of $c_l = 0.4999$ and a drag coefficient of $c_d = 0.005475$. These results also show the AFT-S model's ability to recover the original AFT behavior, with a drag coefficient variation of 0.29% between the two model variants. Lift and drag coefficient evolutions for the deep convergence strategy for the AFT-S variant are shown in Fig. 12.

Even though the ANK solver can converge both AFT and AFT-S models, we observe some key differences in the residuals convergence for both versions. When using the engineering convergence strategy, the flat residuals for the original AFT model after 6000 nonlinear iterations are likely caused by the solution stalling. The discontinuous functions, part of the AFT model, switch back and forth, causing the Newton solver to stop making progress. In this case, the solution updates assume a zero value, and the solver cannot make further progress. In the AFT-S simulations, the smooth functions help the solver to progress further without stalling. The high-frequency residual oscillations observed for the AFT-S model when using the engineering convergence strategy represent variations around a converged state and, therefore, they do not significantly impact the aerodynamic coefficients. Oscillations in residuals are often caused by error modes reflecting in the domain, and smooth physics models do not necessarily prevent these oscillations. We also observe that, with both convergence strategies, the oscillations in the early stages of convergence are less pronounced with the smooth version. This is usually better for Newton-based solvers. When using the deep convergence strategy, we can converge both models to machine-zero residual levels. For other flow cases, we observed similar behavior when using the AFT-S model: when high-frequency oscillations appear in the residuals, they do not substantially affect the lift and drag coefficients. Another relevant aspect is that the smooth functions embedded in the AFT-S solver will likely improve the residuals convergence when a solver other than a Newton-based one is used. When performing gradient-based optimization, discontinu-

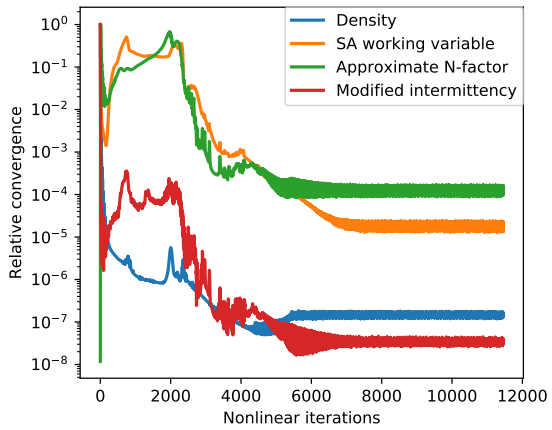

(a) Engineering convergence strategy - AFT-S

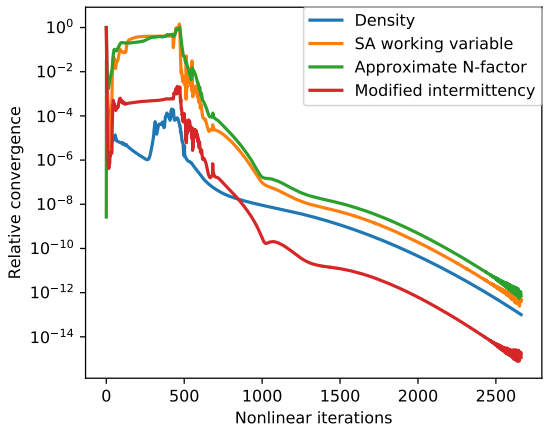

(b) Deep convergence strategy - AFT-S

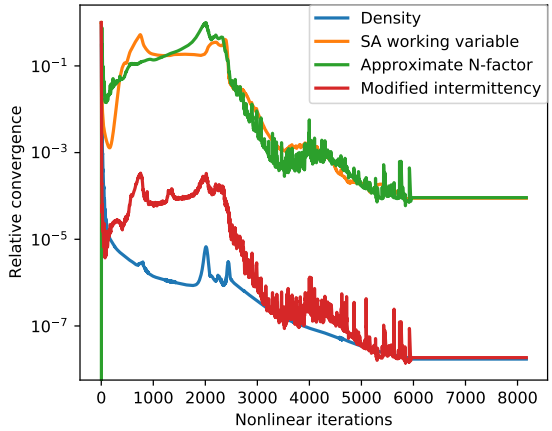

(c) Engineering convergence strategy - AFT

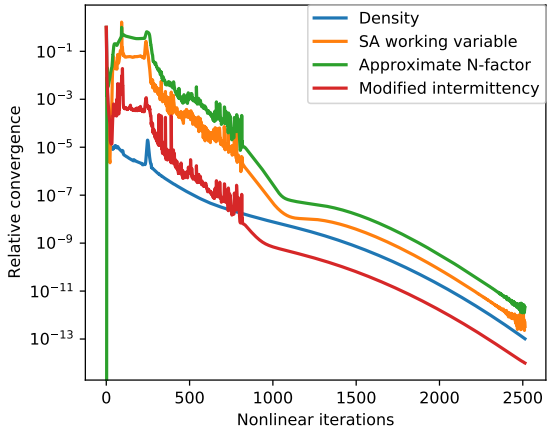

(d) Deep convergence strategy - AFT

Figure 11: Residual convergence histories for the engineering convergence and the deep convergence strategies.

ous functions can introduce discontinuities in the objectives and gradients. A smooth version is preferred for that application regardless of solver performance. In our investigations applying the AFT-S model to gradient-based aerodynamic shape optimization, we observed a good behavior in the adjoint convergence, leading to acceptable gradients. This resulted in the optimizer being able to perform natural laminar flow airfoil optimization [23].

The increased number of sub-iterations for the turbulence subsystem in the deep convergence strategy, combined with a frequent turbulent PC update, increases the computational cost for each nonlinear iteration for both AFT-S and AFT models. The use of larger stencils, contained in the $\mathcal{R}_0$ residual level, also increases the cost. Therefore, the total computational cost of performing the 2660 nonlinear iterations in the deep convergence strategy is 4.4 times larger than the one corresponding to the 10000 nonlinear iterations used in the engineering convergence strategy for the AFT-S model, with a similar factor for the AFT model. For a given convergence

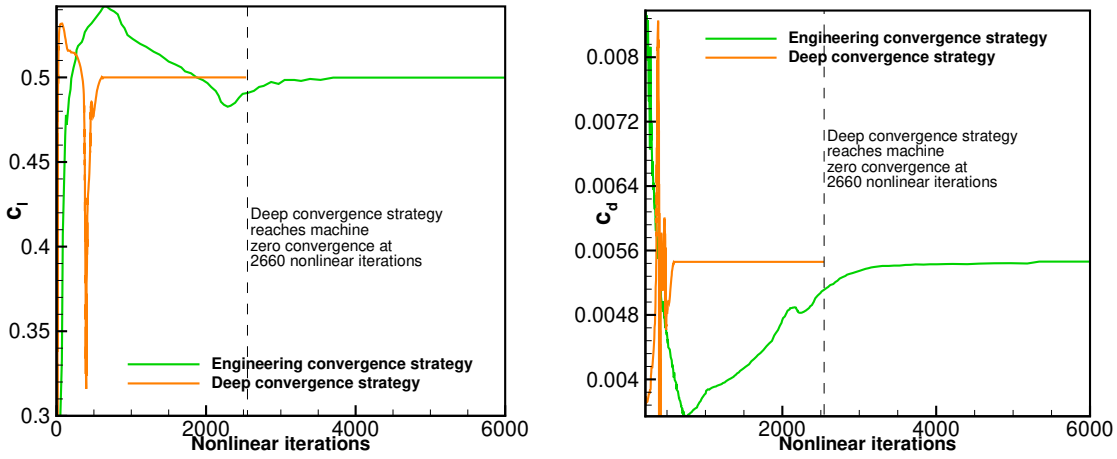

(a) c_l (b) c_d

Figure 12: Lift and drag coefficients convergence histories for both flow solver strategies for the AFT-S model.

strategy, the wall times are comparable when using the AFT or the AFT-S models. The results shown here indicate only a 0.055% difference in drag coefficient between the two strategies proposed here for the AFT-S variant. For the original AFT model, this difference was of 0.018%. This suggests that a trade-off between convergence level and computational time should be exercised when preparing a simulation with transition to turbulence in an ANK solver. Skin friction and pressure coefficients for both flow strategies are indistinguishable, and their distributions are shown in Fig. 13 for the AFT-S model. The close resemblance between skin friction and pressure coefficient

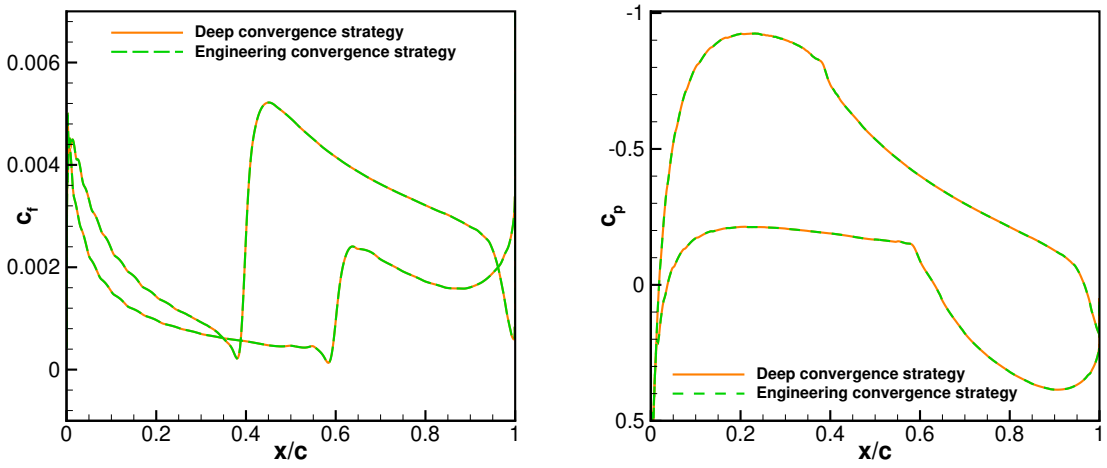

(a) c_f (b) c_p

Figure 13: Skin friction and pressure coefficient distributions for both flow solver strategies for the AFT-S model.

distributions observed in Fig. 13 explains the closely similar drag and identical lift coefficients when comparing numerical results from strategies 1 and 2. This holds for both AFT-S and AFT models. For CFD analysis, this observation leads to an initial conclusion that the additional convergence level provided by the deep convergence strategy does not play a fundamental role in the correct transitional flow prediction.

The numerical methods behind the ANK solver can converge AFT-type models, which are highly nonlinear and contain discontinuous functions that feed the production terms and may present convergence robustness issues. In this section, we illustrated how the ANK solver can be used to converge the AFT-S and AFT transition models. We provide two flow solver settings that lead to distinct residual convergence levels and explore how convergence level impacts the aerodynamic coefficients prediction. While Yang and Mavriplis [52] present interesting results on the machine zero convergence of the AFT model for an airfoil case, they do not explore the model's numerical behavior in depth. To the best of the authors' knowledge, the results presented in this paper constitute the first in-depth investigation of the numerical behavior of an AFT-type transition model. The AFT-S model, which uses smooth surrogate functions to replace original discontinuous relations, retains the physical and numerical behavior of the original AFT model. Additionally, the AFT-S model is compatible with gradient-based optimization and is amenable to algorithmic differentiation, which can be used to compute derivatives. The reverse mode of algorithmic differentiation is equivalent to the adjoint method applied to computer programs [53]. We successfully used the AFT-S model to perform adjoint-based natural laminar flow airfoil optimization in previous work [23]. Even though the ANK solver can converge both the smooth and original versions of the AFT model, we point out that the smooth functions may be helpful to achieve better convergence using distinct solvers, an example being the study of Piotrowski and Zingg [19], who used smooth functions to improve the convergence of a Langtry–Menter-type transition model.

6 Conclusions

The inclusion of transition to turbulence effects in CFD simulations is a required step toward designing natural laminar flow airframes. Because transitional flow also appears in airframes not designed to sustain extended laminar flow regions, CFD tools that include these effects also present better agreement with experimental data than those that use fully turbulent approaches. One example is the study of high-lift elements, where transition is commonly observed.

Modified RANS models that consider transition effects gained momentum in the last decade. The interest in these models lies in the possibility of computing laminar and turbulent flow regions using the same CFD tool without the need to resort to external modules based on flow stability theory or simplified methods. The AFT model uses transport equations for the approximate N-factor and the modified intermittency. These equations are added to the SA turbulence model. The resulting model can predict transition to turbulence caused by the amplification of TS waves.

These modified RANS models usually present challenges related to convergence:

The flow solver cannot decrease the residuals, which generally present high-frequency noise in the residual norm convergence history. In this paper, we modified an ANK solver to converge the meanflow and transition-turbulence systems in a segregated manner. We replaced discontinuous functions in the original AFT model and introduced the AFT-S variant. This is important for making the original model fully compatible with gradient-based aerodynamic shape optimization. We used the AFT-S transition model to investigate transitional flows over airfoils in the subsonic regime and compared the results with those obtained with the original AFT model. Our results indicated that the model can reproduce the transition front dependence on the freestream turbulence intensity observed in experiments. We also showed that transition to turbulence effects increase the agreement with experimental data for cases where transition was detected in the wind tunnel runs. We presented results for a three-dimensional case based on the prolate spheroid configuration and compared our results with experimental data for a flow condition representing TS-dominated transition to turbulence. The AFT-S model proved to be able to capture the transition front in this complex flow scenario correctly.

We proposed two distinct flow solver strategies to converge the AFT-S and AFT transition models transport equations. To the best of the authors' knowledge, only one conference paper has previously provided information on the machine zero convergence characteristics of the original AFT model. Still, no further explorations on this vital topic are available in the literature. The engineering convergence strategy presents an initial decay in the residuals, followed by a plateau. In contrast, the deep convergence strategy can converge the meanflow and turbulence systems down to machine-zero levels. The computational cost for the deep convergence strategy is 4.4 times higher than the one corresponding to the engineering convergence strategy when using AFT-S, with a similar factor for the AFT model. However, both cases reproduce the experimental data well, with drag coefficients that are only different by 0.055% when the AFT-S variant is used and by 0.018% for the original AFT model. This suggests that the partially converged case can be used to perform CFD analysis for flows that present transition to turbulence. Future research will address techniques to increase the efficiency observed in the convergence process. Both strategies proposed herein are considerably more expensive than the fully-turbulent simulations using the SA turbulence model. Future studies will also expand the results presented in this paper to CF-dominated cases.

Acknowledgments

The authors gratefully acknowledge the support provided by Conselho Nacional de Desenvolvimento Científico e Tecnológico, CNPq, Brazil, Research Grant 205552/2014-5. The first author would like to thank Marie Denison (NASA Ames), Scott Murman (NASA Ames) for the discussions on the AFT model and for the assistance with the generation of the results for the prolate spheroid test case. The first author also acknowledges James Coder (University of Tennessee, Knoxville) for the insightful discussions on the AFT model and Michael Piotrowski (University of Toronto) for the

productive conversations on the convergence characteristics of transitional RANS models. This work used the Extreme Science and Engineering Discovery Environment (XSEDE), which is supported by National Science Foundation grant number ACI-1548562. This work also benefited from simulations performed at the NASA Advanced Supercomputing (NAS) Division at Ames research center.

References

[1] Halila, G. L. O., Fidkowski, K. J., and Martins, J. R. R. A., "Toward Automatic Parabolized Stability Equation-Based Transition-to-Turbulence Prediction for Aerodynamic Flows," *AIAA Journal*, Vol. 59, No. 2, February 2021, pp. 462–473.

[2] Halila, G. L. O., Chen, G., Shi, Y., Fidkowski, K. J., Martins, J. R. R. A., and de Mendonça, M. T., "High-Reynolds Number Transitional Flow Simulation via Parabolized Stability Equations with an Adaptive RANS Solver," *Aerospace Science and Technology*, Vol. 91, August 2019, pp. 321–336.

[3] Halila, G. L. O., Bigarella, E. D. V., and Azevedo, J. L. F., "A Numerical Study on Transitional Flows Using a Correlation-Based Transition Model," *Journal of Aircraft*, Vol. 53, No. 4, Jul.–Aug. 2016, pp. 922–941.

[4] Abu-Ghannam, B. J. and Shaw, R., "Natural Transition of Boundary Layers—The Effects of Turbulence, Pressure Gradient and Flow History," *Journal of Mechanical Engineering Science*, Vol. 22, No. 5, 1980, pp. 213–228.

[5] Mayle, R. E., "The Role of Laminar-Turbulent Transition in Gas Turbine Engines," *Journal of Turbomachinery*, Vol. 113, No. 4, 1991, pp. 1–28.

[6] Suzen, Y. B., Huang, P. G., Hultgren, L. S., and Ashpis, D. E., "Predictions of Separated and Transitional Boundary-Layers Under Low-Pressure Turbine Airfoil Conditions Using an Intermittency Transport Equation," *Journal of Turbomachinery*, Vol. 125, No. 3, Jul. 2003, pp. 455–464.

[7] Menter, F. R., Esch, T., S., and Kubacki, "Transition Modeling Based on Local Variables," *5th International Symposium on Turbulence Modeling and Measurements*, Spain, 2002.

[8] Menter, F. R., Langtry, R. B., Likki, S. R., Suzen, Y. B., Huang, P., and Völker, S., "A Correlation-Based Transition Model Using Local Variables—Part I: Model Formulation," *Journal of Turbomachinery*, Vol. 128, No. 3, July 2006, pp. 413–422.

[9] Langtry, R. B., Menter, F. R., Likki, S. R., Suzen, Y. B., Huang, P., and Völker, S., "A Correlation-Based Transition Model Using Local Variables—Part II: Test Cases and Industrial Applications," *Journal of Turbomachinery*, Vol. 128, No. 3, July 2006, pp. 423–434.

[10] Langtry, R. B. and Menter, F. R., "Correlation-Based Transition Modeling for Unstructured Parallelized Computational Fluid Dynamics Codes," *AIAA Journal*, Vol. 47, No. 12, 2009, pp. 2894–2906.

[11] Menter, F. R., "Two-equation eddy-viscosity turbulence models for engineering applications," *AIAA Journal*, Vol. 32, No. 8, 1994, pp. 1598–1605.

[12] Coder, J. G. and Maughmer, M. D., "Computational Fluid Dynamics Compatible Transition Modeling Using an Amplification Factor Transport Equation," *AIAA Journal*, Vol. 52, No. 11, 2014, pp. 2506–2512.

[13] Drela, M. and Giles, M. B., "Viscous-Inviscid Analysis of Transonic and Low Reynolds Number Airfoils," *Journal of Aircraft*, Vol. 25, No. 10, 1987, pp. 1347–1355.

[14] Spalart, P. and Allmaras, S., "A One-Equation Turbulence Model for Aerodynamic Flows," *30th Aerospace Sciences Meeting and Exhibit*, June 1992.

[15] Coder, J. G., "Further Development of the Amplification Factor Transport Transition Model for Aerodynamic Flows," *Proceedings of the AIAA Scitech 2019 Forum*, San Diego, CA., January 2019.

[16] Spalart, P. R. and Rumsey, C. L., "Effective Inflow Conditions for Turbulence Models in Aerodynamic Calculations," *AIAA Journal*, Vol. 45, No. 10, Oct. 2007, pp. 2544–2553.

[17] Halila, G. L. O., Bigarella, E. D. V., Antunes, A. P., and Azevedo, J. L. F., "An Efficient Setup for Freestream Turbulence on Transition Prediction over Aerospace Configurations," *Aerospace Science and Technology*, Vol. 81, October 2018, pp. 259–271.

[18] Denison, M. and Pulliam, T. H., "Implementation and Assessment of the Amplification Factor Transport Laminar-Turbulent Transition Model," *Proceedings of the AIAA Fluid Dynamics Conference, AIAA Aviation Forum*, Atlanta, GA, June 2018.

[19] Piotrowski, M. G. H. and Zingg, D. W., "Smooth Local Correlation-Based Transition Model for the Spalart–Allmaras Turbulence Model," *AIAA Journal*, Vol. 59, No. 2, February 2021.

[20] Mosahebi, A. and Laurendeau, E., "Convergence Characteristics of Fully and Loosely Coupled Numerical Approaches for Transition Models," *AIAA Journal*, Vol. 53, No. 5, May 2015, pp. 1399–1404.

[21] Mosahebi, A. and Laurendeau, E., "Introduction of a modified segregated numerical approach for efficient simulation of γ - Re_θ transition model," *International Journal of Computational Fluid Dynamics*, Vol. 29, No. 5-8, November 2015, pp. 357–375.

[22] Yildirim, A., Kenway, G. K. W., Mader, C. A., and Martins, J. R. R. A., "A Jacobian-free approximate Newton–Krylov startup strategy for RANS simulations," *Journal of Computational Physics*, Vol. 397, November 2019, pp. 108741.

[23] Halila, G. L. O., Martins, J. R. R. A., and Fidkowski, K. J., "Adjoint-Based Aerodynamic Shape Optimization Including Transition to Turbulence Effects," *Aerospace Science and Technology*, , No. 107, December 2020, pp. 106243.

[24] Coder, J. G., Pulliam, T. H., Hue, D., Kenway, G. K. W., and Sclafani, A. J., "Contributions to the 6th AIAA CFD Drag Prediction Workshop Using Structured Grid Methods," *AIAA SciTech Forum*, American Institute of Aeronautics and Astronautics, January 2017.

[25] Coder, J. G., Pulliam, T. H., and Jensen, J. C., "Contributions to HiLIftPW-3 Using Structured, Overset Grid Methods," *Proceedings of the AIAA Aerospace Sciences Meeting, AIAA SciTech Forum*, Kissimmee, FL, January 2018.

[26] Mack, L. M., "Transition Prediction and Linear Stability Theory," AGARD Report CP224, 1977.

[27] Kreisselmeier, G. and Steinhauser, R., "Systematic Control Design by Optimizing a Vector Performance Index," *International Federation of Active Controls Symposium on Computer-Aided Design of Control Systems, Zurich, Switzerland*, 1979.

[28] Poon, N. M. K. and Martins, J. R. R. A., "An Adaptive Approach to Constraint Aggregation Using Adjoint Sensitivity Analysis," *Structural and Multidisciplinary Optimization*, Vol. 34, No. 1, July 2007, pp. 61–73.

[29] Kennedy, G. J. and Hicken, J. E., "Improved constraint-aggregation methods," *Computer Methods in Applied Mechanics and Engineering*, Vol. 289, 2015, pp. 332–354.

[30] Lambe, A. B., Martins, J. R. R. A., and Kennedy, G. J., "An Evaluation of Constraint Aggregation Strategies for Wing Box Mass Minimization," *Structural and Multidisciplinary Optimization*, Vol. 55, No. 1, January 2017, pp. 257–277.

[31] Mader, C. A., Kenway, G. K. W., Yildirim, A., and Martins, J. R. R. A., "ADflow: An open-source computational fluid dynamics solver for aerodynamic and multidisciplinary optimization," *Journal of Aerospace Information Systems*, Vol. 17, No. 9, September 2020, pp. 508–527.

[32] Jameson, A., Schmidt, W., and Turkel, E., "Numerical Solution of the Euler Equations by Finite Volume Methods Using Runge–Kutta Time Stepping Schemes," *14th Fluid and Plasma Dynamics Conference*, No. AIAA 1981-1259, 1981.

[33] Turkel, E. and Vatsa, V. N., "Effects of Artificial Viscosity on Three-Dimensional Flow Solutions," *AIAA Journal*, Vol. 32, 1994, pp. 39–45.

[34] van Leer, B., "Towards the ultimate conservative difference scheme. V. A second-order sequel to Godunov's method," *Journal of Computational Physics*, Vol. 32, 1979, pp. 101–136.

[35] Roe, P. L., "Approximate Riemann Solvers, Parameter Vectors, and Difference Schemes," *Journal of Computational Physics*, Vol. 43, 1981, pp. 357–372.

[36] Klopfer, G., Hung, C., Van der Wijngaart, R., and Onufer, J., "A diagonalized diagonal dominant alternating direction implicit (D3ADI) scheme and subiteration correction," *29th AIAA, Fluid Dynamics Conference, Albuquerque, NM*, June 1998.

[37] Nemec, M. and Zingg, D. W., "Newton–Krylov Algorithm for Aerodynamic Design Using the Navier–Stokes Equations," *AIAA Journal*, Vol. 40, No. 6, June 2002, pp. 1146–1154.

[38] Yildirim, A., Gray, J. S., Mader, C. A., and Martins, J. R. R. A., "Aeropropulsive Design Optimization of a Boundary Layer Ingestion System," *AIAA Aviation Forum*, Dallas, TX, June 2019.

[39] Ceze, M. and Fidkowski, K. J., "Constrained pseudo-transient continuation," *International Journal for Numerical Methods in Engineering*, Vol. 102, No. 11, June 2015, pp. 1683–1703.

[40] Gregory, N. and O'Reilly, "Low-Speed Aerodynamic Characteristics of NACA0012 Airfoil Section Including the Effects of Upper Surface Roughness Simulating Hoar Frost," NLP TR-3276, Aeronautical Research Council, London, England, UK, January 1970.

[41] Coder, J. G., "Standard Test Cases for Transition Model Verification and Validation in Computational Fluid Dynamics," AIAA Paper No. 2018-0029*, Proceedings of the 2018 AIAA Aerospace Sciences Meeting, AIAA SciTech Forum*, Kissimmee, FL, Jan. 2018.

[42] Halila, G. L. O., Bigarella, E. D. V., Antunes, A. P., and Azevedo, J. L. F., "Inflow Turbulence Effects on Transition Prediction Using a Correlation-Based Transition Model," AIAA Paper No. 2016-0550*, Proceedings of the 54rd AIAA Aerospace Sciences Meeting*, San Diego, CA, Jan. 2016.

[43] Arnal, D., "Practical Transition Prediction Methods: Subsonic and Transonic Flows," Advances in Laminar Turbulent Transition Modeling. The Lecture Series of the von Karman Institute, 2008.

[44] Somers, D. M., "Design and Experimental Results for a Flapped Natural-Laminar-Flow Airfoil for General Aviation Applications," Technical report, NASA Langley Research Center, Hampton, VA, United States, 1981, NASA-TP-1865.

[45] Coder, J. G., "Enhancement of the Amplification Factor Transport Transition Modeling Framework," *55th AIAA Aerospace Sciences Meeting*, 2017, pp. 1–14.

[46] Kreplin, H. P., Vollmers, H., and Meier, H., "Wall shear stress measurements on an inclined prolate spheroid in the DFVLR 3m x 3m low speed wind tunnel," Tech. rep., Von Karman Institute for Fluid Dynamics, Göttingen, 1985, Tech. Rep. IB-22-84-A-33, DFVLR-AVA.

[47] Grabe, C. and Krumbein, A., "Correlation-Based Transition Transport Modeling for Three-Dimensional Aerodynamic Configurations," *Journal of Aircraft*, Vol. 50, No. 5, September-October 2013, pp. 1533–1539.

[48] Turkel, E., Vatsa, V. N., and Radespiel, R., "Preconditioning Methods for Low-Speed Flows," *14th AIAA Applied Aerodynamics Conference*, American Institute of Aeronautics and Astronautics, New Orleans, LA, June 1996, pp. 650–660.

[49] Lian, C., Xia, G., and Merkle, C. L., "Impact of Source Terms on Reliability of CFD Algorithms," *Computers and Fluids*, Vol. 10, December 2010, pp. 1909–1922.

[50] Mavriplis, D. J., Ahrabi, B., and Brazell, M., "Strategies for Accelerating Newton Method Continuation in CFD Problems," *Proceedings of the AIAA Scitech 2019 Forum*, AIAA, San Diego, CA, January 2019.

[51] Mavriplis, D., Yang, Z., and Anderson, E. M., "Adjoint Based Optimization of a Slotted Natural Laminar Flow Wing for Ultra Efficient Flight," *Proceedings of the AIAA Scitech 2020 Forum*, Orlando, FL, January 2020.

[52] Yang, Z. and Mavriplis, D. J., "Discrete Adjoint Formulation for Turbulent Flow Problems with Transition Modelling on Unstructured Meshes," *AIAA SciTech Forum*, San Diego, CA, Jan. 2019.

[53] Martins, J. R. R. A. and Ning, A., *Engineering Design Optimization*, Cambridge University Press, 2021.